Supporting Information

Kellner et al. 10.1073/pnas.1407086111

SI Methods

Sample Preparation. One single-cysteine variant (rhodanese K174C) and five different double-cysteine variants of rhodanese (Δ39 K135C/K174C, Δ49 K236C/E285C, Δ58 E77C/K135C, Δ117 D102C/D219C, and Δ159 E77C/K236C) were produced by site-directed mutagenesis. The rhodanese variants were prepared as previously described for wild-type rhodanese (1). All five double-cysteine rhodanese variants were labeled with Alexa Fluor 488 and Alexa Fluor 594 as described before (2), whereas rhodanese K174C was labeled with Alexa Fluor 488 C5 maleimide (Invitrogen, Molecular Probes) according to the manufacturer's instructions using maleimide-thiol chemistry. Briefly, a twofold molar excess of Alexa Flour 488 and Alexa Flour 594 maleimide derivatives was added to the protein. After 1 h of incubation at room temperature, unreacted dye was removed by gel filtration. Variants Δ39 and Δ117 contained a large fraction of doubly Alexa 488-labeled molecules. A large part of this incorrectly labeled species was removed by anion exchange chromatography, which was performed on an ÄKTA purifier FPLC system with a MonoQ 5/50 GL column (GE Healthcare). For the Δ117 variant, the system was equilibrated in 10 mM Tris·HCl buffer, pH 8.5, and eluted with a gradient from 0 to 200 mM sodium chloride over 60 mL (12 column volumes). The Δ39 variant was purified in 50 mM Tris·HCl, pH 7.0, and eluted with a gradient from 0 to 500 mM sodium chloride over 60 mL (12 column volumes). To test the structural integrity of the fluorophore-labeled rhodanese variants, their enzymatic activity was determined as described by Westley (3). The labeled rhodanese variants exhibited an activity similar to wild-type rhodanese (wild-type: 0.9 mmol min^{-1} mg^{-1}, Δ39: 1.0 mmol min^{-1} mg^{-1}, Δ49: 0.5 mmol min^{-1} mg^{-1}, Δ58: 0.6 mmol min^{-1} mg^{-1}, and Δ117: 0.6 mmol min^{-1} mg^{-1}). DnaK, DnaJ, and GrpE were gifts from H.-J. Schönfeld (Hoffmann-La Roche Ltd., Basel). The concentrations of the stock solutions were 100 μM for DnaK and DnaJ and 200 μM for GrpE in 50 mM Tris·HCl, pH 7.7, and 100 mM NaCl.

To form rhodanese–chaperone complexes, rhodanese was denatured in 4 M guanidinium chloride (GdmCl) in buffer A (50 mM Tris·HCl, 10 mM $MgCl_2$, 5 mM KCl, 200 mM β-mercaptoethanol, and 0.001% Tween 20) and refolded by 100× dilution into buffer A in the absence of GdmCl and in the presence of DnaK, DnaJ, GrpE, and nucleotides at the indicated concentrations directly before the measurements. The final rhodanese concentration was between 25 and 75 pM. Native rhodanese was measured in buffer A; denatured rhodanese under native conditions was measured in the microfluidic mixing device described below.

Single-Molecule Fluorescence Spectroscopy. Single-molecule FRET (smFRET) measurements were performed at 22 °C using either a MicroTime 200 confocal microscope (PicoQuant) or a custom-built confocal microscope. Both instruments use pulsed interleaved excitation (4). Pulses for acceptor excitation were generated by a SC450-PP super continuum fiber laser (Fianium) operating at a 20-MHz repetition rate. The wavelength was selected with a z582/15 band-pass filter (Chroma Technology), and the power, measured at the back aperture of the microscope objective, was set to 35 μW; 483-nm donor excitation pulses (100 μW at the back aperture) were obtained from an LDH-D-C-485 diode laser (PicoQuant). The driving electronics of the diode laser (Sepia II; PicoQuant) were triggered by infrared light of the Fianium laser detected on a fast photodiode (DET10a/M; Thorlabs). The lasers were focused into the sample solutions with a UPlanApo 60x/1.20W objective (Olympus). The fluorescence signal passed a chromatic beam splitter (R405/488/594 or z488/568; Chroma Technology) and a 100-μm pinhole before further distribution according to polarization (polarizing beam splitter cube) and wavelength (dichroic mirrors 595 DCXR or 585 DCXR; Chroma Technology) onto four detection channels equipped with avalanche photodiodes. Before detection, the emission was finally filtered by ET525/50M or HQ650/100 band-pass filters (Chroma Technology) for donor and acceptor fluorescence, respectively. Time-correlated single-photon counting electronics (HydraHarp 400; PicoQuant) recorded each photon detection pulse with 16-ps time resolution.

The brightness of the rhodanese–chaperone complexes was determined by measuring the fluorescence emission of ∼2 nM singly labeled rhodanese K174C-Alexa 488 alone or in complex with DnaJ (0.5 μM DnaJ) or DnaK (10 μM DnaK, 0.5 μM DnaJ, and 1 mM ATP) on the confocal microscope. The fluorophore was excited at 485 nm with 100 μW at 40 MHz with the diode laser, and only one detector was used.

Data Reduction. Only photons detected after donor excitation pulses were used for construction of FRET efficiency histograms, whereas photons after acceptor excitation pulses were used to probe whether a molecule carried an active acceptor fluorophore. Successive photons with interphoton times of less than 150 μs detected in any channel following donor excitation pulses were combined into one photon burst. Only bursts containing more than 35 photons after correction for background, differences in quantum yields of the fluorophores, different collection efficiencies of the detection channels, cross-talk, and direct excitation of the acceptor (5) were used for further analysis. Bursts with a significant likelihood for acceptor photobleaching were excluded from further analysis as described previously (6). Transfer efficiencies were calculated for each burst from $E = n_A/(n_D + n_A)$, where n_D and n_A are the corrected donor and acceptor counts detected after donor excitation, respectively (5). Bursts were further analyzed for the stoichiometry ratio (7), $S = n_{Dexc}/(n_{Dexc} + n_{Aexc})$, where n_{Dexc} is the total number of counts after the donor excitation and n_{Aexc} is the total number of counts after acceptor excitation. Molecules lacking an active acceptor dye yield a stoichiometry ratio close to 1 and were excluded from FRET efficiency histograms. Histograms were constructed with a bin width of 0.03.

To quantify the kinetics of conformational changes on the timescale of minutes and longer, moving window analysis was used (8). We constructed series of FRET efficiency histograms from long single-molecule measurements (0.5–2 h) by splitting them into overlapping intervals of 5-min duration starting every 100 s. FRET efficiency histograms obtained from the bursts of each interval were constructed and represented as lines in time-resolved FRET efficiency histograms (FRET kinetics) in which the color indicates the time, increasing from blue to green.

Donor fluorescence anisotropies were determined from photons arriving at the donor detectors after 485-nm excitation and acceptor anisotropies from photons arriving at the acceptor detectors after 590-nm acceptor direct excitation. The G-factor of the instrument (a correction for different detection efficiencies for parallel and perpendicular polarized light) was calibrated to be 1.245 by comparison of ensemble fluorescence anisotropy measurements with measurements at the confocal smFRET setup of free dye in water and 50% glycerol. To account for the optical path and the high-numerical-aperture objective in the confocal setup, additional correction factors were determined according to Koshioka et al. (9). We found the correction factors to be $L_1 = 0.098$

and $L_2 = 0.094$ for 485-nm excitation and $L_1 = 0.111$ and $L_2 = 0.058$ for 590-nm excitation. Anisotropies were calculated as

$$r = \frac{I_{\parallel} - G\, I_{\perp}}{(1 - 3\, L_2)\, I_{\parallel} + (2 - 3\, L_1)\, G\, I_{\perp}}, \quad \textbf{[S1]}$$

where $I_{\parallel}$ and $I_{\perp}$ denote the fluorescence intensity for parallel and perpendicular polarized light with respect to the polarization of the excitation light, respectively (Table S2).

Microfluidic Mixing. For probing kinetics on timescales shorter than minutes, we used the microfluidic mixing device described in detail by Wunderlich et al. (10). To observe the association of DnaK with DnaJ–rhodanese complexes, DnaJ–rhodanese Δ39 complexes were preformed as described above with a final concentration of 0.55 μM DnaJ and with 22 μM ATP. This solution was supplied to the side channels of the microfluidic device and mixed with 100 μM DnaK (50 mM Tris·HCl, pH 7.7, and 100 mM NaCl) present in the central channel. The mixer was operated at a flow velocity of 1 mm/s (fully developed flow in the observation channel) and at a mixing ratio of 1:9 to obtain final concentrations in the observation channel of 10 μM DnaK, 20 μM ATP, and 0.5 μM DnaJ. These conditions were obtained by applying 15.1 kPa (2.19 psi) and 16.1 kPa (2.33 psi) at the main and side inlet channels, respectively. The concentration of Tween 20 in buffer A was increased to 0.01% to prevent nonspecific interactions of the chaperone–substrate complexes with the polydimethylsiloxane surfaces of the microfluidic mixing channels. The confocal volume was focused into the observation channel at different positions downstream from the mixing region, corresponding to different times after mixing. Fluorescence bursts were detected at each position for 30 min. Positions were converted to times after mixing as described by Wunderlich et al. (11). Histograms were obtained for 1, 5, 7.5, 10, 20, 30, 40, and 50 s after mixing.

Transfer efficiency histograms of denatured rhodanese under native conditions (buffer A with 0.4 M GdmCl) were obtained by mixing denatured rhodanese in 4 M GdmCl (central channel) with buffer A (side channels) at an average flow rate of 0.8 mm/s in the observation channel and placing the confocal volume at a position 100 μm (125 ms) downstream of the mixing region. The applied pressures were 10.4 kPa (1.5 psi) in the side channels and 6.8 kPa (1 psi) in the central channel.

For combining manual and microfluidic mixing smFRET experiments (Fig. 3) the transfer efficiency histograms were normalized by the total number of bursts. Fractions of bursts with transfer efficiencies from 0.0 to 0.3 and 0.6 to 0.8 were used for monitoring the progress of the DnaK complex and DnaJ complex interconversion. The two curves were fitted globally to double exponential decays with common rate constants, yielding $k_1 = 0.028\ s^{-1}$ and $k_2 = 0.002\ s^{-1}$.

Dual-Focus Fluorescence Correlation Spectroscopy. Dual-focus fluorescence correlation spectroscopy (2f-FCS) measurements were performed at 22 °C on a MicroTime 200 confocal microscope equipped with a Nomarski prism (12). Two orthogonally polarized diode lasers at 483 nm (LDH-D-C-485; PicoQuant) with repetition rates of 20 MHz and laser powers of 30 μW (at the back aperture of the microscope objective) each were used to excite the sample alternatingly. The emission light passed through a 150-μm pinhole and was focused onto the detectors (tau-SPAD50; PicoQuant). The distance between the two foci was measured to be 440 ± 10 nm as described previously (13). All 2f-FCS experiments were performed with rhodanese K174C Alexa 488 at a final concentration of 0.5 nM. The auto- and cross-correlation functions of both foci were analyzed globally as described by Dertinger et al. (12), and the resulting translational diffusion coefficients, D, were converted into Stokes radii (R_S) using the Stokes–Einstein equation (14), where k_B is the Boltzmann constant, T the temperature, and η the solvent viscosity:

$$R_S = \frac{k_B T}{6\,\pi\,\eta\,D}. \quad \textbf{[S2]}$$

Bimolecular Association Rate of DnaJ and Denatured Rhodanese. Assuming that unfolded rhodanese will partition to its native conformation or bind to DnaJ as shown in Fig. S1*A*, we estimated the bimolecular association rate coefficient, $k_{on,DnaJ}$, for the DnaJ–rhodanese complex from the fraction of native rhodanese, f_N, after dilution of unfolded protein in the presence of DnaJ according to

$$k_{on,\,DnaJ} = \frac{\frac{1 - f_N}{f_N} k_{fold}}{[DnaJ]}. \quad \textbf{[S3]}$$

The folding rate constants, k_{fold}, of the variants were determined from independent kinetic measurements where unfolded rhodanese was diluted into native buffer in the absence of chaperones (Fig. S1*C*). A single-exponential rise was fitted to the change of the number of bursts within the transfer efficiency range corresponding to the native subpopulations (Fig. S1*F* and Table S1). f_N was estimated from smFRET measurements of rhodanese after dilution into native buffer in the absence (Fig. S1*D*) and presence (Fig. S1*E*) of 0.5 μM DnaJ. The data in Fig. S1*D* were fitted with a Gaussian. Subsequently, the data in Fig. S1*E* were fitted with Gaussians with identical positions and widths. The values of f_N were estimated from a comparison of the amplitudes of the fitted Gaussians (Table S1).

Estimation of the Stoichiometry of DnaJ–Rhodanese Complexes. The R_S of rhodanese and DnaJ–rhodanese complexes formed at 0.5 μM DnaJ were determined from five independent 2f-FCS measurements. Assuming a spherical shape, the molecular weight (MW) of a complex was estimated (Eq. **S4**) from R_S, where we used the average molar mass of amino acids $m_{aa} = 111$ g/mol (weighted for their abundance in proteins) (15) and the average Stokes volume of an amino acid $\upsilon_{aa} = 0.27\ nm^3$ (Table S3) (13, 16):

$$MW = \rho V_S = \frac{m_{aa}}{\nu_{aa}} \frac{4\,\pi}{3} R_S^3. \quad \textbf{[S4]}$$

υ_{aa} was determined as follows. For a compact chain with a spherical shape, the radius of gyration, R_G, and the R_S are related by

$$R_G = \sqrt{\frac{3}{5}} R_S. \quad \textbf{[S5]}$$

R_G and R_S scale with the number of amino acid residues N according to

$$R_G = a\, N^{\frac{1}{3}} \quad \textbf{[S6]}$$

and

$$R_S = b\, N^{\frac{1}{3}}. \quad \textbf{[S7]}$$

Dima and Thirumalai (16) determined $a = 0.3$ nm from ∼400 PDB structures of monomeric globular proteins, thus $b = 0.4$ nm. This value is in good agreement with $b = 0.47$ nm obtained by Wilkins et al. (17). Finally, υ_{aa} is given by

$$\nu_{aa} = \frac{4\,\pi}{3} b^3. \quad \textbf{[S8]}$$

Molecular Dynamics Simulations of Rhodanese Bound to Different Numbers of DnaK Molecules. Protein structures were simplified using one bead per amino acid corresponding to the position of the Cα atom. Unfolded rhodanese was modeled using a flexible local potential (AICG2 in CafeMol) dependent on the amino acid sequence that was shown to reasonably reproduce the conformational distribution of unfolded states or intrinsically disordered proteins (18). An additional potential term, accounting for intrachain hydrophobic interactions, was added to better reproduce the compact unfolded state of rhodanese under native conditions. This multibody potential term (HP in CafeMol) depends on the surface exposure of each amino acid (19) and its weight was tuned to obtain a radius of gyration for unfolded rhodanese close to what was determined by smFRET experiments.

DnaK was modeled with a structure-based model (20) using the NMR structure of *Escherichia coli* DnaK complexed with ADP and substrate (PDB ID code 2KHO) as a reference conformation. Nonbonded native interactions involving residues in the flexible interdomain linker were switched off and the AICG2 potential was used to model this region. Using this setup, it was possible to limit the conformational flexibility of the individual domains while allowing significant fluctuations of the interdomain arrangement in agreement with NMR residual dipolar coupling analysis (21).

To model DnaK–rhodanese complexes, the substrate peptide present in the NMR structure of ADP-bound DnaK was replaced by the corresponding part of an extended rhodanese chain. Artificial harmonic restraints were imposed on the interresidue distances between the rhodanese chain and DnaK binding residues to preserve the binding arrangement. Apart from these restraints, the interactions between rhodanese and DnaK molecules were limited to excluded volume effects.

Seven potential DnaK binding sites were identified in the rhodanese sequence according to the predictor proposed by Van Durme et al. (22). [Another algorithm by Rüdiger et al. (23) yielded similar binding sites; Fig. S4.] This resulted in seven possible stoichiometries (rhodanese:$DnaK_N$ with n = 1–7) and a total of $(2^7 - 1) = 127$ possible distinct molecular complexes. Each individual complex was simulated using Langevin dynamics with a temperature T = 300 K for ∼108 time steps with an integration step size of 0.1 t, where t corresponds to CafeMol time units (t ∼200 fs) (24). Only the configurations corresponding to the second half of each trajectory were used to calculate the distance distributions reported in Fig. 2.

R_G and end-to-end distance distributions for the simulated rhodanese–$DnaK_N$ complexes were calculated from the simulation results and are represented in Table S4. Distance distributions for polypeptide chain segments on the rhodanese chain corresponding to the label positions of the rhodanese variants used in smFRET experiments were extracted and converted to transfer efficiencies with

$$\langle E\rangle_{simulation} = \sum P(r)\,E(r)dr. \qquad \textbf{[S9]}$$

Stokes radii were estimated from simulation snapshots with HydroPro (25) calculations based on a bead model where each residue corresponded to an element with a R_S equal to 6.1 Å. The harmonic average of the results corresponding to each stoichiometry was then used for estimating the mean R_S reported in Table S4.

Mean Transfer Efficiency, Mean Interdye Distance, End-To-End Distances, and Radii of Gyration of DnaK–Rhodanese Complexes from smFRET Histograms. Analyzing the FRET efficiency histograms of rhodanese–DnaK complexes in terms of quantitative distance distributions is complicated by the static and dynamic heterogeneity of the system. The broadening beyond shot noise indicates interconversion between different conformations or rhodanese/DnaK stoichiometries on the millisecond timescale and/or above, but faster reconfiguration dynamics are likely to be present also. Note, however, that the average transfer efficiencies of the subpopulations corresponding to the rhodanese–DnaK complexes are independent of these dynamics as long as they interconvert slowly on the fluorescence lifetime of the dyes (26), which is a reasonable assumption because this applies even to unfolded and intrinsically disordered proteins in the absence of bound chaperones (27, 28). Given the only moderately high anisotropies of the fluorophores (Table S2), a pronounced effect of the orientational distribution on the transfer efficiencies is unlikely (29).

We therefore use the following procedure. The mean transfer efficiencies of the DnaK–rhodanese complexes were determined from the histograms of rhodanese in the presence of 10 μM DnaK, 0.5 μM DnaJ, and 1 mM ATP (Fig. 1*E*). To account for the residual population of rhodanese molecules that are not bound by DnaK but are either folded or bound to DnaJ, the histograms were fitted to the sum of a log-normal function, $P(E)$, and an interpolation function obtained from the histograms in the presence of DnaJ (Fig. 1*D*). The mean transfer efficiencies, $\langle E\rangle$, of the DnaK–rhodanese complexes were then calculated from

$$\langle E\rangle = \int_{-0.2}^{1.2} P(E)\,E\,dE \Big/ \int_{-0.2}^{1.2} P(E)\,dE \qquad \textbf{[S10]}$$

and converted to root mean square interdye distances, $\langle r^2\rangle^{1/2}$, by numerically solving Eq. **S11**:

$$\langle E\rangle = \int P(r)\,E(r)\,dr \Big/ \int P(r)\,dr. \qquad \textbf{[S11]}$$

We assume normal distributions for $P(r)$ (Eq. **S12**) because they provide a good approximation of the distance distributions observed in the simulations of the rhodanese–DnaK complexes (Fig. 2*B*):

$$P(r) = \frac{1}{\sqrt{2\pi\ \sigma^2}} e^{-\frac{(r-\langle r\rangle)^2}{2\sigma^2}}. \qquad \textbf{[S12]}$$

The lowest overall mean square deviation between the average transfer efficiencies of all rhodanese variants obtained from the smFRET experiments and the simulations is observed for six DnaK molecules bound (N_{DnaK} = 6) (Fig. 2*C*). The values of σ in Eq. **S12** were thus taken from the fits of normal distributions to the interdye distance distributions obtained from the molecular dynamics (MD) simulations of six DnaK (N_{DnaK}) molecules bound to rhodanese. The distance dependence of the transfer efficiency is given by the Förster equation (Eq. **S13**) with the Förster radius R_0 = 5.4 nm for Alexa 488 and Alexa 594 (30):

$$E(r) = \frac{1}{1 + (r/R_0)^6}. \qquad \textbf{[S13]}$$

To estimate, from the intramolecular distance distributions of the different rhodanese variants determined in this way, the average end-to-end distance of rhodanese in complex with DnaK, we use the scaling of the average intramolecular distance with the sequence separation of the labeling positions obtained from the simulations. First, the average interdye distance, $\langle r\rangle$, as a function of the amino acid sequence separation between the label positions, Δaa, from the MD simulations of the different numbers of DnaK molecules bound to rhodanese was fit to

$$\langle r\rangle(\Delta aa) = g\,\Delta aa^x. \qquad \textbf{[S14]}$$

For N_{DnaK} = 6, a scaling exponent of x = 0.71 was obtained. Eq. **S14** with x = 0.71 was then used to fit the interdye distances from the experimental data as function of the sequence separation and

extrapolated to the average end-to-end distance, $\langle r_{ee} \rangle$, of rhodanese in complex with DnaK, yielding $\langle r_{ee} \rangle = 17.3 \pm 0.3$ nm. The uncertainty of the extrapolation was estimated by varying x in the range obtained for $N_{DnaK} = 5$ to $N_{DnaK} = 7$. Finally, we used the average ratio $R_G/\langle r_{ee} \rangle$ calculated from the simulations for $N_{DnaK} = 5$ to $N_{DnaK} = 7$, 2.4 ± 0.1, to convert the experimental value of $\langle r_{ee} \rangle$ to $R_G = 7.2 \pm 0.3$ nm (Table S4).

Dissociation of the DnaK–Rhodanese Complex at Single-Turnover ATP Concentrations. To determine the dissociation rate constant of DnaK and rhodanese, DnaK–rhodanese complexes were formed at 0.5 μM DnaJ, 10 μM DnaK, and 10 μM ATP (i.e., equimolar concentrations of DnaK and ATP). The subsequent dissociation of the complex was observed by smFRET measurements for 30 min (Fig. 4*B*). The total numbers of bursts observed per time interval were determined for all variants (Fig. 4*C*), and the resulting decays in burst numbers were fitted with a single-exponential function. The mean of the five rate constants obtained (Table S1) is $k_{diss,\ DnaK} = (2.5 \pm 0.4)\ 10^{-3}\ s^{-1}$. The kinetics of the change in R_S determined from 2f-FCS measurements (Fig. 4*A*) yielded $k_{diss,\ DnaK} = (1.7 \pm 0.4)\ 10^{-3}\ s^{-1}$.

1. Miller DM, et al. (1992) Recombinant bovine rhodanese: Purification and comparison with bovine liver rhodanese. *Biochim Biophys Acta* 1121(3):286–292.
2. Hillger F, Nettels D, Dorsch S, Schuler B (2007) Detection and analysis of protein aggregation with confocal single molecule fluorescence spectroscopy. *J Fluoresc* 17(6):759–765.
3. Westley J (1981) Thiosulfate: Cyanide sulfurtransferase (rhodanese). *Methods Enzymol* 77:285–291.
4. Müller BK, Zaychikov E, Bräuchle C, Lamb DC (2005) Pulsed interleaved excitation. *Biophys J* 89(5):3508–3522.
5. Schuler B (2007) Application of single molecule Förster resonance energy transfer to protein folding. *Methods Mol Biol* 350:115–138.
6. Kudryavtsev V, et al. (2012) Combining MFD and PIE for accurate single-pair Förster resonance energy transfer measurements. *ChemPhysChem* 13(4):1060–1078.
7. Kapanidis AN, et al. (2004) Fluorescence-aided molecule sorting: Analysis of structure and interactions by alternating-laser excitation of single molecules. *Proc Natl Acad Sci USA* 101(24):8936–8941.
8. Hofmann H, et al. (2010) Single-molecule spectroscopy of protein folding in a chaperonin cage. *Proc Natl Acad Sci USA* 107(26):11793–11798.
9. Koshioka M, Sasaki K, Masuhara H (1995) Time-dependent fluorescence depolarization analysis in 3-dimensional microspectroscopy. *Appl. Spect.* 49(2):224–228.
10. Wunderlich B, et al. (2013) Microfluidic mixer designed for performing single-molecule kinetics with confocal detection on timescales from milliseconds to minutes. *Nat Protoc* 8(8):1459–1474.
11. Wunderlich B, Nettels D, Schuler B (2014) Taylor dispersion and the position-to-time conversion in microfluidic mixing devices. *Lab Chip* 14(1):219–228.
12. Dertinger T, et al. (2007) Two-focus fluorescence correlation spectroscopy: A new tool for accurate and absolute diffusion measurements. *ChemPhysChem* 8(3):433–443.
13. Hofmann H, et al. (2012) Polymer scaling laws of unfolded and intrinsically disordered proteins quantified with single-molecule spectroscopy. *Proc Natl Acad Sci USA* 109(40):16155–16160.
14. Einstein A (1905) The motion of elements suspended in static liquids as claimed in the molecular kinetic theory of heat. *Ann Phys-Berlin* 17(8):549–560.
15. Jordan IK, et al. (2005) A universal trend of amino acid gain and loss in protein evolution. *Nature* 433(7026):633–638.
16. Dima RI, Thirumalai D (2004) Asymmetry in the shapes of folded and denatured states of proteins. *J Phys Chem B* 108(21):6564–6570.
17. Wilkins DK, et al. (1999) Hydrodynamic radii of native and denatured proteins measured by pulse field gradient NMR techniques. *Biochemistry* 38(50): 16424–16431.
18. Terakawa T, Takada S (2011) Multiscale ensemble modeling of intrinsically disordered proteins: p53 N-terminal domain. *Biophys J* 101(6):1450–1458.
19. Fujitsuka Y, Takada S, Luthey-Schulten ZA, Wolynes PG (2004) Optimizing physical energy functions for protein folding. *Proteins* 54(1):88–103.
20. Clementi C, Nymeyer H, Onuchic JN (2000) Topological and energetic factors: What determines the structural details of the transition state ensemble and "en-route" intermediates for protein folding? An investigation for small globular proteins. *J Mol Biol* 298(5):937–953.
21. Bertelsen EB, Chang L, Gestwicki JE, Zuiderweg ERP (2009) Solution conformation of wild-type E. coli Hsp70 (DnaK) chaperone complexed with ADP and substrate. *Proc Natl Acad Sci USA* 106(21):8471–8476.
22. Van Durme J, et al. (2009) Accurate prediction of DnaK-peptide binding via homology modelling and experimental data. *PLOS Comput Biol* 5(8):e1000475.
23. Rüdiger S, Germeroth L, Schneider-Mergener J, Bukau B (1997) Substrate specificity of the DnaK chaperone determined by screening cellulose-bound peptide libraries. *EMBO J* 16(7):1501–1507.
24. Kenzaki H, et al. (2011) CafeMol: A coarse-grained biomolecular simulator for simulating proteins at work. *J Chem Theory Comput* 7(6):1979–1989.
25. Ortega A, Amorós D, García de la Torre J (2011) Prediction of hydrodynamic and other solution properties of rigid proteins from atomic- and residue-level models. *Biophys J* 101(4):892–898.
26. Schuler B, Lipman EA, Steinbach PJ, Kumke M, Eaton WA (2005) Polyproline and the "spectroscopic ruler" revisited with single-molecule fluorescence. *Proc Natl Acad Sci USA* 102(8):2754–2759.
27. Soranno A, et al. (2012) Quantifying internal friction in unfolded and intrinsically disordered proteins with single-molecule spectroscopy. *Proc Natl Acad Sci USA* 109(44):17800–17806.
28. Nettels D, Gopich IV, Hoffmann A, Schuler B (2007) Ultrafast dynamics of protein collapse from single-molecule photon statistics. *Proc Natl Acad Sci USA* 104(8):2655–2660.
29. Hillger F, et al. (2008) Probing protein-chaperone interactions with single-molecule fluorescence spectroscopy. *Angew Chem Int Ed Engl* 47(33):6184–6188.
30. Schuler B, Lipman EA, Eaton WA (2002) Probing the free-energy surface for protein folding with single-molecule fluorescence spectroscopy. *Nature* 419(6908):743–747.

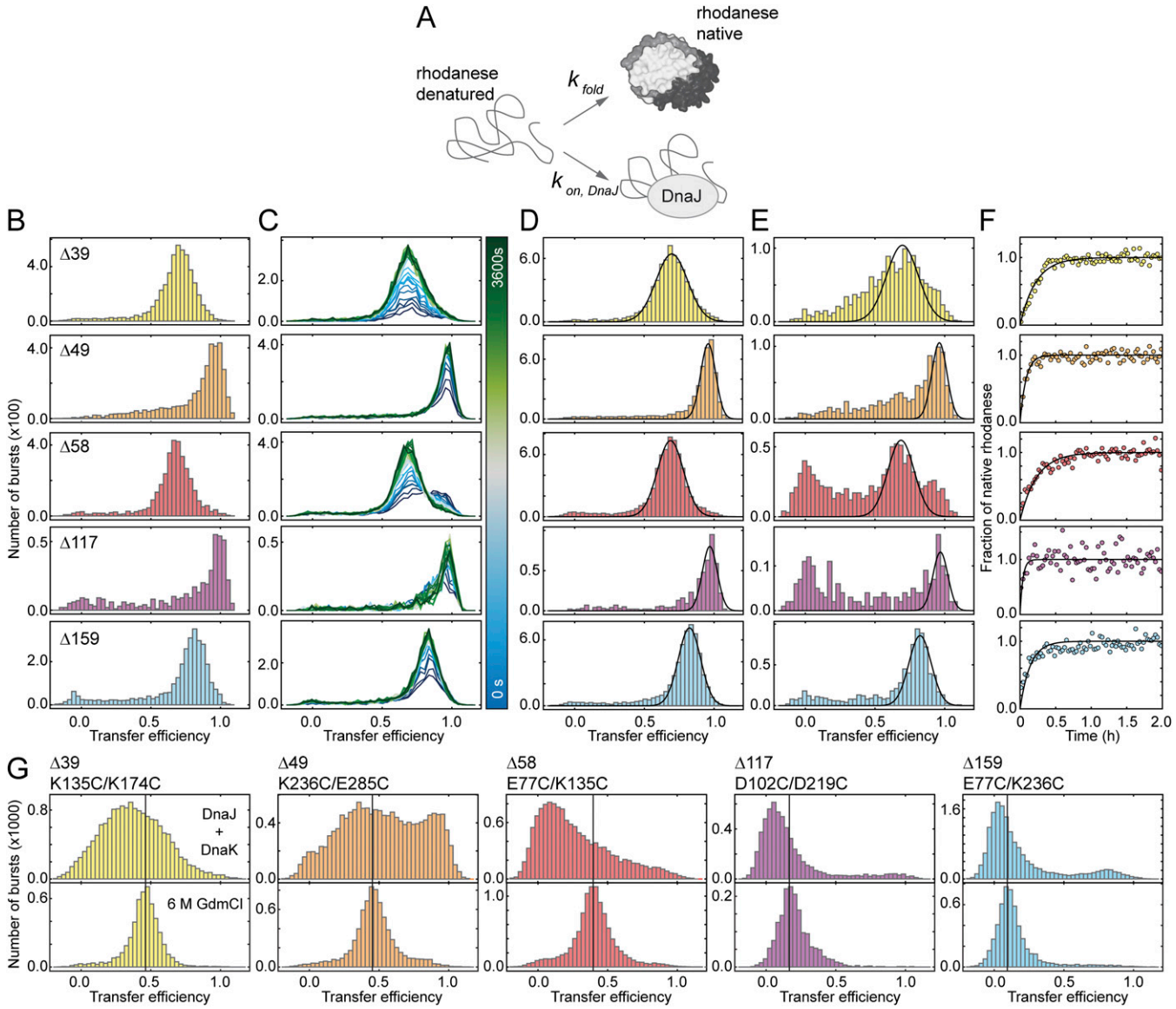

Fig. S1. Refolding of rhodanese in the absence and presence of the co-chaperone DnaJ for estimation of the bimolecular association rate coefficient for the formation of DnaJ–rhodanese complexes. (*A*) Kinetic model used for the determination of $k_{on,DnaJ}$. (*B*) Transfer efficiency histograms of native rhodanese variants. Each histogram was recorded for 5 min. (*C*) FRET kinetics of refolding rhodanese (1 h of measurement time is shown). (*D*) Transfer efficiency histograms of native rhodanese after complete refolding in absence of chaperones. Histograms are constructed from the last 10 min of the 2-h measurements represented in *C*. The native populations were fitted with Gaussian peaks (black lines). (*E*) Transfer efficiency histograms of rhodanese after refolding in the presence of 0.5 μM DnaJ. Histograms are constructed from 10-min measurements recorded 50 min after dilution into native buffer. Gaussian peaks with the same positions and widths as in *C* were used to estimate the native-state subpopulations (black lines). The small populations at zero transfer efficiency in *E* (note the axis scaling and the small amplitudes of this population compared with *D*) originate from incomplete elimination of molecules with inactive acceptor fluorophores by pulsed interleaved excitation. (*F*) Refolding of rhodanese under single-molecule conditions observed as an increase in the fraction of native protein from data in *C*. Black lines indicate single exponential fits. (*G*) Comparison of the transfer efficiency histograms of rhodanese in the presence of 6 M GdmCl (*Lower*) and in complex with 10 μM DnaK (in the presence of 0.5 μM DnaJ, 1 mM ATP; *Upper*). The black vertical lines indicate the transfer efficiency maxima of the rhodanese variants denatured in 6 M GdmCl.

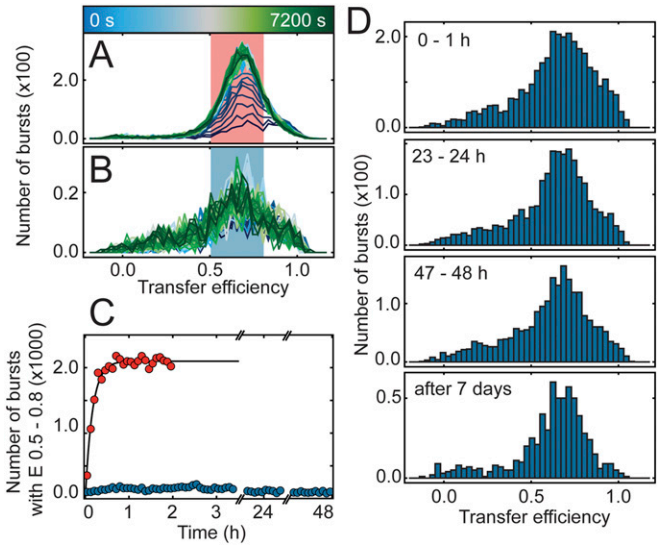

Fig. S2. Stability of DnaJ–rhodanese complexes. Refolding of rhodanese Δ39 in the absence (*A*) and presence (*B*) of 0.5 μM DnaJ. The FRET kinetics were obtained from 2-h measurements. (*C*) Number of bursts per time interval (5 min) in the absence (red) and presence of 0.5 μM DnaJ (blue) observed within a transfer efficiency range from 0.5 to 0.8 (shaded regions in *A* and *B*). (*D*) Representative transfer efficiency histograms from the kinetic series in *C* (blue).

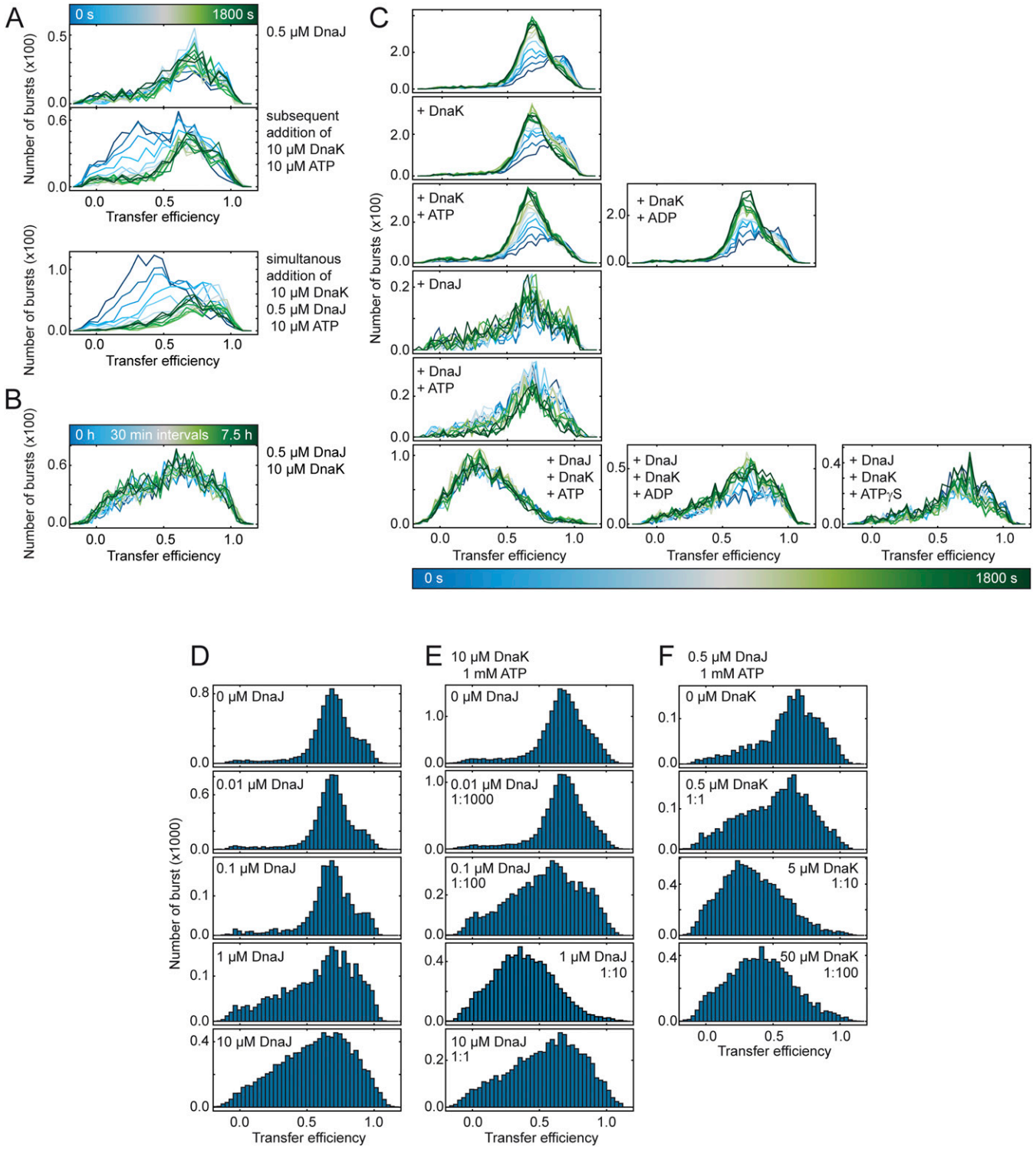

Fig. S3. Formation of the DnaK–rhodanese complex is strictly dependent on the presence of DnaJ and ATP and is modulated by the ratio of DnaJ and DnaK. (*A*) Comparison of FRET kinetics of DnaK (10 µM) and ATP (1 mM) added to preformed DnaJ–rhodanese complexes (refolding of denatured rhodanese Δ39 in the presence of 0.5 µM DnaJ) and DnaK, DnaJ, and ATP added simultaneously to rhodanese Δ39. (*B*) FRET kinetics (7.5 h in 30-min windows) of denatured rhodanese (Δ39) in the presence of 10 µM DnaK and 0.5 µM DnaJ, without nucleotides. (*C*) FRET kinetics (30 min) of refolding rhodanese (Δ39) in the absence and presence of chaperones and nucleotides (concentrations: 10 µM DnaK, 0.5 µM DnaJ, and 1 mM ATP, ADP, or ATPγS). The commercially obtained nucleotides (ADP and ATPγS) were not purified further from possible ATP contaminations because the histograms did not show a low transfer efficiency population that would indicate such a contamination. (*D*) Transfer efficiency histograms of rhodanese (Δ39) from 30-min measurements after refolding in the presence of increasing DnaJ concentrations (*E*) in the presence of 10 µM DnaK, 1 mM ATP, and increasing DnaJ concentrations and (*F*) in the presence of 0.5 µM DnaJ, 1 mM ATP, and increasing concentrations of DnaK. Ratios denote the DnaJ:DnaK ratio.

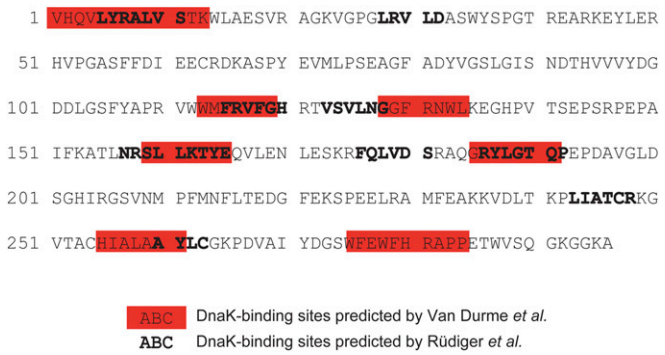

Fig. S4. DnaK binding sites in the rhodanese amino acid sequence. DnaK binding sites were predicted with the LIMBO algorithm by van Durme et al. (22) (red) and with the algorithm of Rüdiger et al. (23) (bold).

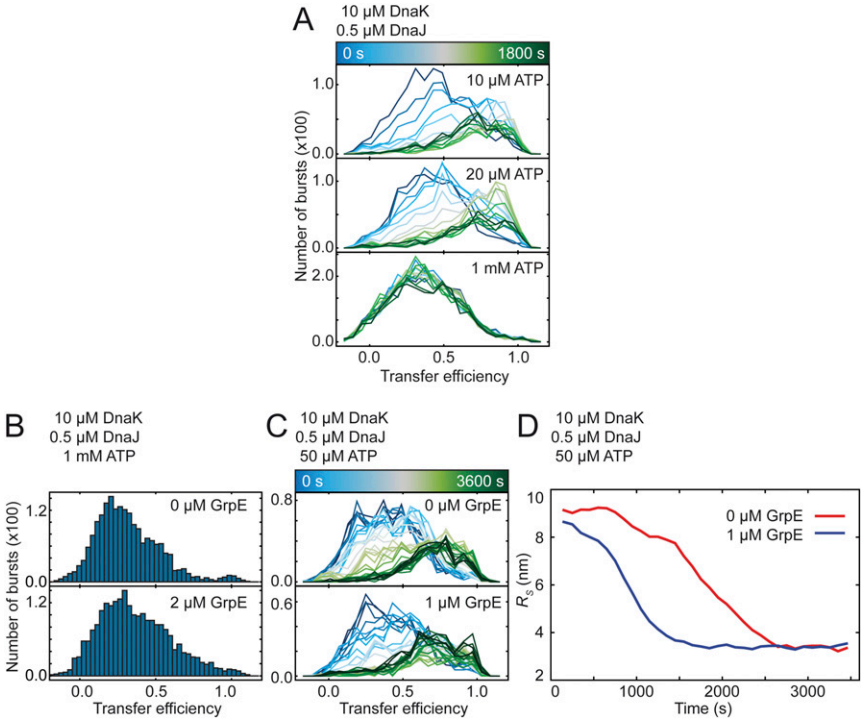

Fig. S5. The concentrations of ATP and GrpE modulate the kinetic stability of rhodanese–DnaK complexes. (*A*) FRET kinetics (30 min) of rhodanese (Δ39) in the presence of 0.5 μM DnaJ, 10 μM DnaK, and ATP at indicated concentrations. (*B*) Transfer efficiency histograms of rhodanese in the presence of 10 μM DnaK, 0.5 μM DnaJ, and 1 mM ATP in the absence and presence of 2 μM GrpE, measured for 30 min. (*C*) FRET kinetics (1 h) of rhodanese (Δ39) in the presence of 0.5 μM DnaJ, 10 μM DnaK, 50 μM ATP, and GrpE as indicated. (*D*) Changes in R_S determined from 2f-FCS measured under the same conditions as in *C*.

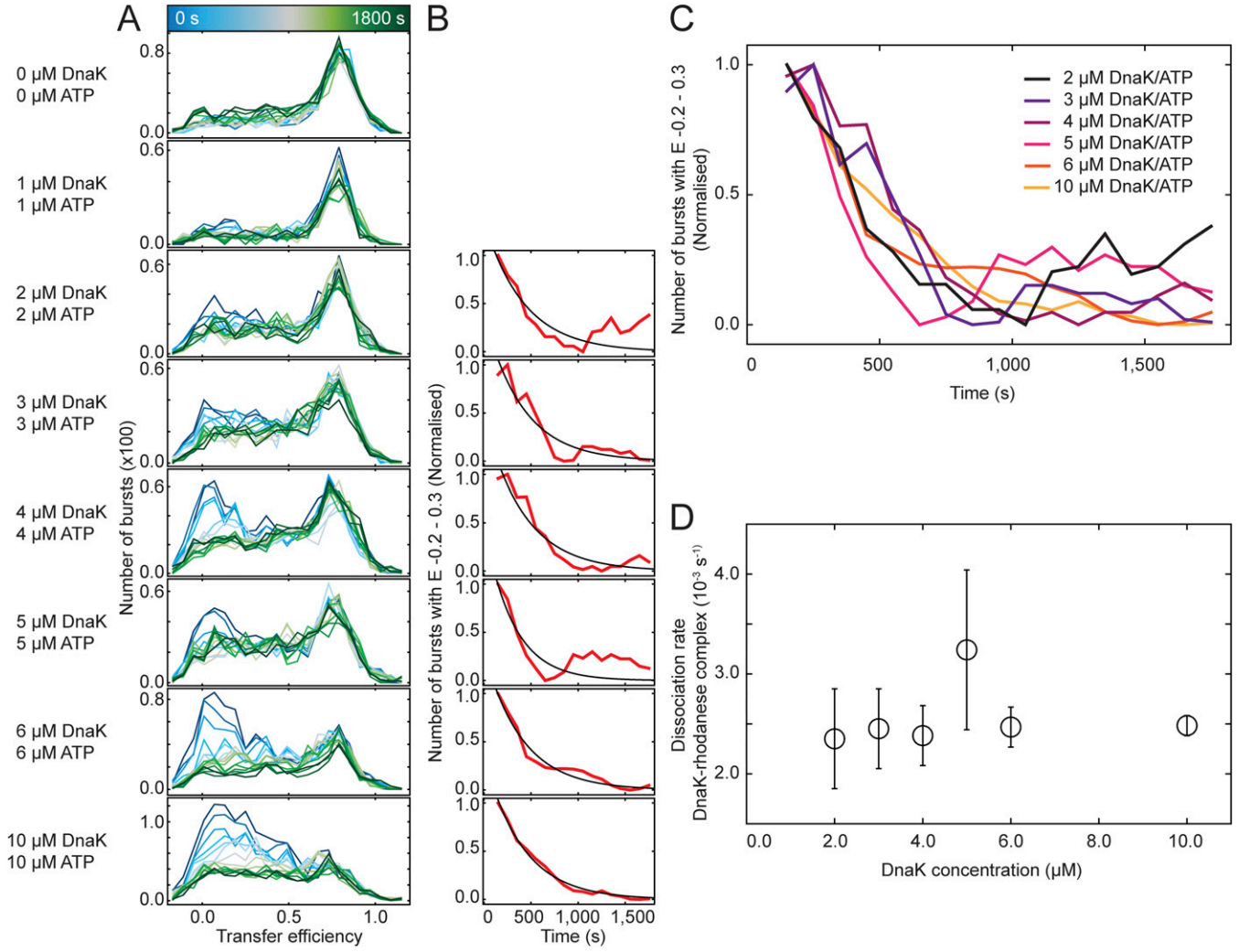

Fig. S6. The dissociation rate of DnaK from DnaK–rhodanese complexes is independent of the DnaK concentration. (*A*) FRET kinetics of DnaK–rhodanese (Δ159) complexes. Complexes are formed in the presence of 0.5 μM DnaJ and equimolar concentrations of DnaK and ATP as indicated. The bin width for the transfer efficiency histograms was 0.06. (*B*) Decrease of the DnaK–rhodanese complex population monitored by the number of bursts with a transfer efficiency < 0.3 (red line, normalized data; black line, single exponential fit). (*C*) Comparison of the datasets from *B*. (*D*) Rate constants from fits in *B* as a function of the DnaK concentration. Error bars indicate the error of the fit.

Table S1. Kinetic parameters of DnaJ and DnaK–rhodanese complexes

Rhodanese variant	Transfer efficiency (native population)	k_{fold}, s^{-1}	f_n	$k_{on,\ DnaJ}$, $s^{-1}\ M^{-1}$	$k_{diss,\ DnaK}$, s^{-1}
K135C/K174C	0.60–0.80	0.001	0.2	1.3×10^4	2.6×10^{-3}
K236C/K285C	0.85–1.05	0.003	0.1	4.2×10^4	1.8×10^{-3}
E77C/K135C	0.55–0.75	0.001	0.1	2.9×10^4	2.7×10^{-3}
D102C/D219C	0.85–1.05	0.007	0.2	7.3×10^4	3.0×10^{-3}
E77C/K236C	0.75–0.95	0.002	0.1	2.8×10^4	2.4×10^{-3}
Mean				$(3.7 \pm 2.2) \times 10^4$	$(2.5 \pm 0.4) \times 10^{-3}$
Global fit					$(2.4 \pm 0.1) \times 10^{-3}$

Determination of the association rate constant, $k_{on,\ DnaJ}$, for the DnaJ–rhodanese complex from FRET kinetics experiments (Fig. S1) and for the dissociation rate constant, $k_{diss,\ DnaK}$, of DnaK and rhodanese at 10 μM DnaK, 0.5 μM DnaJ, and 10 μM ATP from FRET kinetics (Fig. 4). k_{fold} is the folding rate constant of rhodanese and f_N the fraction of native rhodanese molecules (Fig. S1).

Table S2. Steady-state anisotropies of Alexa 488 and Alexa 594 and brightness of Alexa 488 bound to rhodanese (Δ39 or rhodanese K174C Alexa 488) in complex with DnaJ (0.5 μM DnaJ) or DnaK (0.5 μM DnaJ, 10 μM DnaK, and 1 mM ATP) or native without chaperones

Molecular species	Anisotropy Alexa 488	Anisotropy Alexa 594	Brightness, cps
Native rhodanese	0.15	0.24	8.9×10^4
DnaJ–rhodanese complex	0.22	0.28	1.3×10^4
DnaK–rhodanese complex	0.21	0.25	5.6×10^4

Table S3. Comparison of theoretical and experimental Stokes radii, R_S, and molecular masses of DnaJ–rhodanese complexes (DnaJ molecules counted as monomers) of different stoichiometries estimated from Eq. S4

Theoretical values	Rhodanese	Rhodanese + 1 DnaJ	Rhodanese + 2 DnaJ	Rhodanese + 3 DnaJ	Rhodanese + 4 DnaJ
Molecular mass (kD)	33	74	115	156	197
Stokes Radius R_S (nm) from Eq. **S4**	2.7	3.5	4.1	4.5	4.9

Experimental values (2f-FCS)	Rhodanese	DnaJ – rhodanese complex
Measured R_S (nm)	2.6 ± 0.1	3.1 ± 0.2
Molecular mass (kD) from Eq. **S4**	30	51

Table S4. Stokes radii, R_S, (HydroPro) (25), average end-to-end distances, $\langle r_{ee} \rangle$, and radii of gyration, R_G, for rhodanese in complex with different numbers of DnaK molecules from MD simulations and estimation of R_G for single-molecule FRET experiments based on the shape of the distance distributions from the MD simulations

N_{DnaK}	$\langle r_{ee} \rangle$ simulation, nm	R_G simulation, nm	$\langle r_{ee} \rangle / R_G$ simulation	R_G experiment, nm	R_S simulation, nm
0					3.6
1					5.2
2					6.3
3					7.2
4					8.0
5	21.0	9.2	2.3	7.5	8.8
6	23.3	9.6	2.4	7.2	9.5
7	24.8	10.0	2.5	6.9	9.9
Mean			2.4 ± 0.1	7.2 ± 0.3	